Interrogation of a ring-resonator ultrasound sensor using a fiber Mach-Zehnder interferometer

Grillo Peternella, Fellipe; Ouyang, Boling; Horsten, Roland; Haverdings, Michael; Kat, Pim; Caro, Jaap

DOI
10.1364/OE.25.031622

Publication date
2017

Document Version
Final published version

Published in
Optics Express

Research Article | Vol. 25, No. 25 | 11 Dec 2017 | OPTICS EXPRESS 31622
Optics EXPRESS

Interrogation of a ring-resonator ultrasound sensor using a fiber Mach-Zehnder interferometer

FELLIPE GRILLO PETERNELLA,[1,*] BOLING OUYANG,[1] ROLAND HORSTEN,[1] MICHAEL HAVERDINGS,[2] PIM KAT,[2] AND JACOB CARO[1]

[1]*Department of Imaging Physics, Delft University of Technology, Lorentzweg 1, 2628 CJ Delft, The Netherlands*
[2]*Technobis tft-fos, Pyrietstraat 2, 1812 SC Alkmaar, The Netherlands*
[*]*F.GrilloPeternella@tudelft.nl*

Abstract: We experimentally demonstrate an interrogation procedure of a ring-resonator ultrasound sensor using a fiber Mach-Zehnder interferometer (MZI). The sensor comprises a silicon ring resonator (RR) located on a silicon-oxide membrane, designed to have its lowest vibrational mode in the MHz range, which is the range of intravascular ultrasound (IVUS) imaging. Ultrasound incident on the membrane excites its vibrational mode and as a result induces a modulation of the resonance wavelength of the RR, which is a measure of the amplitude of the ultrasound waves. The interrogation procedure developed is based on the mathematical description of the interrogator operation presented in Appendix A, where we identify the amplitude of the angular deflection Φ_0 on the circle arc periodically traced in the plane of the two orthogonal interrogator voltages, as the principal sensor signal. Interrogation is demonstrated for two sensors with membrane vibrational modes at 1.3 and 0.77 MHz, by applying continuous wave ultrasound in a wide pressure range. Ultrasound is detected at a pressure as low as 1.2 Pa. Two optical path differences (OPDs) of the MZI are used. Thus, different interference conditions of the optical signals are defined, leading to a higher apparent sensitivity for the larger OPD, which is accompanied by a weaker signal, however. Independent measurements using the modulation method yield a resonance modulation per unit of pressure of 21.4 fm/Pa (sensor #1) and 103.8 fm/Pa (sensor #2).

OCIS codes: (070.5753) Resonators; (120.3180) Interferometry; (130.3120) Integrated optics devices; (130.6010) Sensors; (170.7170) Ultrasound; (220.4241) Nanostructure fabrication.

References and links

1. T. Tsuchizawa, K. Yamada, T. Watanabe, S. Park, H. Nishi, R. Kou, H. Shinojima, and S. Itabashi, "Monolithic integration of silicon, germanium, and silica-based optical devices for telecommunications applications," IEEE J. Sel. Topics Quantum Electron. **17**(3), 516–525 (2011).
2. A. P. Freitas, G. B. Farias, F. G. Peternella, Y. R. R. Bustamante, D. A. Motta, and J. C. R. F. de Oliveira, "112 Gb/s compact silicon-on-insulator coherent receiver," Proc. of SPIE **9390**, 93900D (2015).
3. C. Koos, P. Vorreau, T. Vallaitis, P. Dumon, W. Bogaerts, R. Baets, B. Esembeson, I. Biaggio, T. Michinobu, F. Diederich, W. Freude, and J. Leuthold, "All-optical high-speed signal processing with silicon-organic hybrid slot waveguides," Nat. Photon. **3**(4), 216–219 (2009).
4. V. M. N. Passaro, C. Tullio, B. Troia, M. L. Notte, G. Giannoccaro, and F. De Leonardis, "Recent advances in integrated photonic sensors," Sensors **12**(11), 15558–15598 (2012).
5. A. Dhakal, A. Raza, F. Peyskens, A. Z. Subramanian, S. Clemmen, N. L. Thomas, and R. Baets, "Efficiency of evanescent excitation and collection of spontaneous Raman scattering near high index contrast channel waveguides," Opt. Express **23**(21), 27391–27404 (2015).
6. M. Boerkamp, T. van Leest, J. Heldens, A. Leinse, M. Hoekman, R. Heideman, and J. Caro, "On-chip optical trapping and Raman spectroscopy using a TripleX dual-waveguide trap," Opt. Express **22**(25), 30528–30537 (2014).
7. S. M. Leinders, W. J. Westerveld, J. Pozo, P. L. M .J. van Neer, B. Snyder, P. O'Brien, H. P. Urbach, N. de Jong, and M. D. Verweij, "A sensitive optical micro-machined ultrasound sensor (OMUS) based on a silicon photonic ring

#313828 https://doi.org/10.1364/OE.25.031622
Journal © 2017 Received 20 Nov 2017; accepted 22 Nov 2017; published 5 Dec 2017

Optics EXPRESS

resonator on an acoustical membrane," Sci. Rep. **5**, 14328 (2015).
8. M. Perry, P. Orr, P. Niewczas, M. Johnston, "High-speed interferometric FBG interrogator with dynamic and absolute wavelength measurement capability," J. Lightwave Technol. **31**(17), 2897–2903 (2013).
9. A. Dandridge, "Fiber optic sensors based on the Mach-Zehnder and Michelson Interferometers," in *Fiber Optic Sensors: An Introduction for Engineers and Scientists*, E. Udd, ed. (Wiley, 1991).
10. W. J. Westerveld, S. M. Leinders, P. M. Muilwijk, J. Pozo, T. C. van den Dool, M. D. Verweij, M. Yousefi, H. P. Urbach, "Characterization of integrated optical strain sensors based on silicon waveguides," IEEE J. Sel. Topics Quantum Electron. **20**(4), 5900110 (2014).
11. ePIXfab website http://www.epixfab.eu/, accessed on October 30, 2017.
12. N. Pavarelli, J. S. Lee, M. Rensing, C. Scarcella, S. Zhou, P. Ossieur, and P. A. O'Brien, "Optical and electronic packaging processes for silicon photonic systems," J. Lightwave Technol. **33**(5), 991–997 (2015).
13. E. Hallynck and P. Bienstman, "Integrated optical pressure sensors in silicon-on-insulator," IEEE Photon. J. **4**(2), 450–453 (2012).
14. C. Zhang, S. L. Chen, T. Ling, and L. J. Guo, "Imprinted polymer microrings as high performance ultrasound detectors in photoacoustic imaging," J. Lightwave Technol. **33**(20), 4318–4328 (2015).
15. W. Bogaerts, P. de Heyn, T. van Vaerenbergh, K. DeVos, S. Selvaraja, T. Claes, P. Dumon, P. Bienstman, D. Van Thourhout, and R. Baets, "Silicon microring resonators," Laser Photon. Rev. **6**(1), 47–73 (2012).
16. R. G. Priest, "Analysis of fiber interferometer utilizing 3 3 fiber coupler," IEEE Trans. Microw. Theory Techn. **30**(10), 1589–1591 (1982).
17. Y. Li, "Light beams with flat-topped profiles," Opt. Lett. **27**(12), 1007–1009(2002).
18. A. Dandridge, C. C. Wang, A. B. Tveten, and A. M. Yurek, "Performance of 3x3 couplers in fiber optic sensor systems," Proc. of SPIE **2360**, 549–552 (1994).
19. W. Gander, G. H. Golub, and R. Strebel, "Least-squares fitting for circles and ellipses," BIT Numerical Mathematics **34**(4), 558–578 (1994).
20. J. C. Lagarias, J. A. Reeds, M. H. Wright, and P. E. Wright, "Convergence properties of the Nelder-Mead simplex method in low dimensions," SIAM Journal of Optimization **9**(1), 112–147 (1998).
21. To unwrap the phase we use the function unwrap of MATLAB R2014b, The MathWorks, Inc., Natick, Massachusetts, United States.
22. R. S. Evenblij and J. A. P. Leijtens, "Space gator, a giant leap for fiber optic sensing," online Proceedings of the International Conference on Space Optics, Tenerife, Spain, 6-10 October 2014. Website http://www.icsoproceedings.org/, accessed on June 8, 2017.
23. F. W. J. Olver, "Bessel functions of integer order," in *Handbook of Mathematical Functions with Formulas, Graphs and Mathematical Tables*, M. Abramowitz and I.A. Stegun, eds. (Dover books on Mathematics, 1964).

1. Introduction

Integrated photonics is an enabling technology for important application fields, such as telecommunication [1, 2], optical signal processing [3] and various types of photonic sensing [4]. In the field of sensing the main advantages of integrated photonics sensors are small size, mass producibility, low cost and electromagnetic immunity. The lab-on-chip approach to chemical sensing and particle identification also benefits strongly from integrated photonics. This is demonstrated for example by recent advances in excitation and collection of spontaneous Raman scattering near silicon nitride waveguides [5] and in optical trapping and Raman spectroscopy of micro-particles using a dual-beam trap made from composite silicon oxide-nitride waveguides [6].

In the field of sensing for health and medicine, integrated silicon photonics is used in our department for an ultrasound sensor based on a ring resonator (RR) located on a thin membrane [7]. Ultrasound waves make the membrane vibrate and as a result induce a modulation of the optical resonance wavelength of the RR, which characterizes the waves. The sensor is very promising for medical ultrasound imaging, in particular for intravascular ultrasound (IVUS) imaging, which is widely used to diagnose atherosclerosis in humans. For IVUS, important advantages of our RR ultrasound sensor are its high sensitivity [7], the possibility to realize an array of sensors on a single chip, which is spontaneously enabled by the CMOS fabrication technology, and the absence of electrical wiring as needed for piezoelectric IVUS sensors. Wiring has the disadvantages of being rather cumbersome for an array of piezoelectric sensors and susceptible to cross-talk, while making the sensors incompatible with magnetic resonance imaging.

Here, we present an interrogation procedure of a RR ultrasound sensors of the type introduced in [7] using a passive fiber Mach-Zehnder interferometer [8, 9]. The procedure yields a well-

Optics EXPRESS

defined relation between the sensor signal and the applied ultrasound pressure. For amplitudes of the ultrasound-induced resonance-wavelength modulation smaller than the bandwidth of the spectrum incident on the RR, the signal is proportional to the applied ultrasound pressure. The MZI employs a 3×3 fiber output coupler, of which at least two of the three outputs are non-zero for any optical phase difference between the MZI arms. This is beneficial for the signal-to-noise ratio of the quadrature signal components defined with the three outputs. We demonstrate detection of ultrasound waves of a pressure amplitude as small as 1.2 Pa. A complete mathematical description of the operation of the interrogator, resulting in the interrogation procedure we apply, is given in Appendix A.

2. Silicon ring-resonator sensor for ultrasound

The heart of the ultrasound sensor is a racetrack silicon RR, coupled to bus waveguides as depicted in Fig. 1. The sensor is located on a silicon oxide membrane with its lowest vibrational mode in the MHz range. To mimic the situation of IVUS imaging, the sensor is operated in water. Ultrasound of the proper characteristics incident on the membrane excites the vibrational mode and therefore periodically deforms the RR. Thus, the optical signal is encoded with information of the ultrasound. In particular, the RR resonance wavelength is modulated at the ultrasound frequency. The modulation results from the combined effect [10] of elongation of the ring's straight parts and three other types of change, *viz.* of the ring's cross section, of the refractive indices of the waveguide core and cladding and of the effective index of the ring's mode due to the elasto-optic effect.

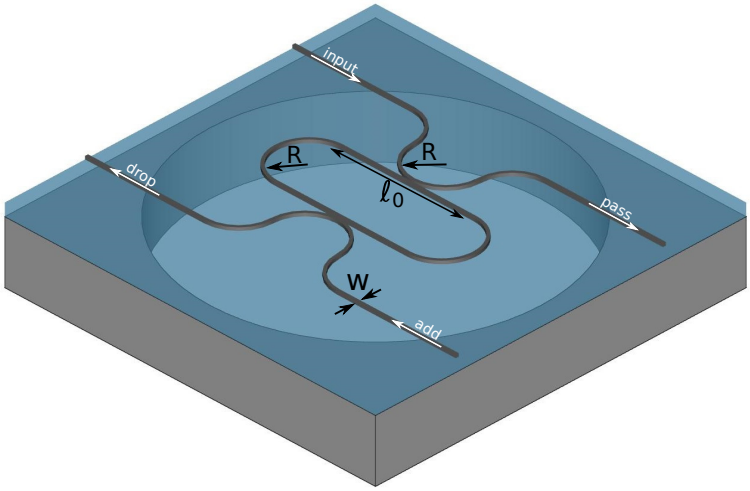

Fig. 1. Schematic view of the silicon ring-resonator sensor fabricated on a circular silicon oxide membrane. Width of coupling waveguides and racetrack is w = 400 nm, while the gap of the directional couplers is 200 nm. Radius of bends is R = 5 μm. The length of the straight part of the racetrack ℓ_0 varies among the devices.

The RRs were fabricated at ePIXfab, Imec [11] on silicon-on-insulator wafers thinned to 250 μm. The silicon device layer and the buried oxide (BOX) layer are 220 nm and 2 μm thick, respectively. The width of the ring and the bus waveguides are 400 nm, implying these are single mode around the operational wavelength of 1550 nm. The gap of the identical directional couplers of the RR is 200 nm. The length ℓ_0 of the straight part of the racetracks is in the range 20-100 μm, while the bend radius is 5 μm. For light coupling from and to external fibers we use grating couplers (GCs), to which 10 μm wide waveguides are connected. The GCs are polarization

Optics EXPRESS

sensitive, implying that the modes coupled into and out of the waveguides and circulating the ring are TE polarized. The 10 μm wide waveguides are adiabatically tapered down to 400 nm in two steps.

The actual sensors result after a post-processing step performed in the Kavli Nanolab Delft. Under a RR a membrane is created by deep reactive ion etching of a circular hole in the handle wafer. Etching from the backside stops selectively at the BOX layer, and thus a membrane is formed. In this procedure, a 2.5 μm PECVD oxide layer is used as a hard mask and the photonic circuitry on the front side is protected by a 0.5 μm thick PECVD oxide layer, also serving as upper cladding. The resulting membranes thus have a thickness of 2.5 μm. The cavity under the membrane is closed by gluing a glass platelet to the chip's backside, entrapping air. The sensor thus operates with a membrane that is water loaded on one side. The fibers are permanently connected to the sensor via angled and aluminium coated Pyrex mirror blocks glued to the chip [12]. Only the pass port is fiber-connected, implying that the transmission spectrum shows a series of dips.

Silicon waveguides have high index contrast, allowing for small bend radii. This is advantageous for small footprint sensors, as recognized before in [13], which reports a silicon RR sensor on a membrane for measurement of static pressures. The RR, however, is still relatively large. Ultrasound detection with polymer RRs is reported in [14]. These RRs are not located on a membrane and thus only rely on the elasto-optic effect. Further, polymer waveguides have a rather low index contrast with respect to the cladding. Therefore, bend radii are more limited than for silicon RRs.

In this article we concentrate on two sensors: sensor #1 with $\ell_0 = 30$ μm located on a 66 μm diameter membrane (vibrational mode at 1.3 MHz) and sensor #2 with $\ell_0 = 40$ μm located on a 124 μm diameter membrane (vibrational mode at 0.77 MHz). For sensor #1, the transmission spectra without applied ultrasound are shown in Fig. 2. The resonance dips captured in Fig. 2(a) give a free spectral range $P_{\mathrm{RR}} = 6.01$ nm. Fig. 2(b) is a zoom-in of the central dip at 1550.19 nm, which we use for experiments with the interrogator (section 4). The setup for measuring the dips is addressed in connection to the modulation method (Appendix B).

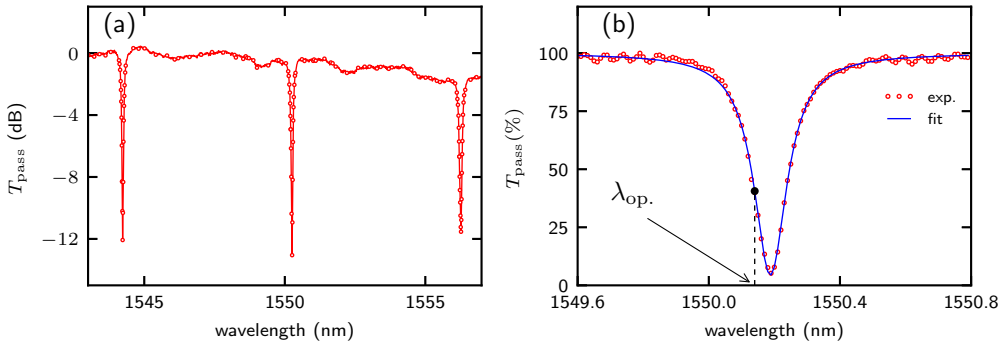

Fig. 2. (a) Transmission spectrum of sensor #1, showing three resonance dips. (b) Zoom-in of the central dip in (a). The blue curve is a fit of Eq. (3) to the data points. On the linear part of the dip's left flank the operation point $\lambda_{\mathrm{op.}}$ is shown, the static wavelength to which the laser is tuned in the modulation method (section 4.2).

To analyze a single resonance, we start from the expression for the transmission to the pass port for two identical directional couplers, which is [15]

$$T_{\mathrm{pass}}(\theta) = \frac{r^2 + r^2a^2 - 2r^2a\cos\theta}{1 + r^4a^2 - 2r^2a\cos\theta}. \tag{1}$$

Optics EXPRESS

Here r is the self-coupling coefficient of the directional coupler, a the single round-trip amplitude transmission, and θ is the accumulated phase of the mode for a single round trip in the ring. When concentrating on a single resonance, the phase can be approximated by

$$\theta = \frac{2\pi}{\lambda} n_{\text{eff}}(\lambda) L \cong 2\pi m - 2\pi n_g L \frac{\lambda - \lambda_r}{\lambda_r^2}. \tag{2}$$

Here λ is the wavelength, λ_r the resonance wavelength, L the round-trip length and m an integer. n_{eff} and n_g are the wavelength dependent effective index and the group index at resonance, respectively. The right-hand side of Eq. (2) results from keeping only the first order term of the Taylor expansion of the function $n_{\text{eff}}(\lambda)/\lambda$ around λ_r and implementing the resonance condition $n_{\text{eff}}(\lambda_r)L = m\lambda_r$. Eq. (1) simplifies further by using $\cos\theta \cong 1 - \theta^2/2$ near the resonance phase $\theta = 2\pi m$, which for the cosine is equivalent to $\theta = 0$, and by using Eq. (2). This yields the single-dip transmission

$$T_{\text{pass}}(\lambda) \approx \frac{(\lambda - \lambda_r)^2 + \varepsilon(\gamma_r/2)^2}{(\lambda - \lambda_r)^2 + (\gamma_r/2)^2}. \tag{3}$$

Here γ_r and ε are defined by, respectively

$$\gamma_r = \frac{\lambda_r^2(1 - ar^2)}{\pi n_g L r\sqrt{a}} = \text{FWHM} \tag{4}$$

$$\varepsilon = \frac{r^2(1-a)^2}{(1-ar^2)^2}. \tag{5}$$

In Eq. (4), γ_r=FWHM is the full width at half minimum of the resonance dip. The line shape function of Eq. (3) corresponds to $[1 - (1 - \varepsilon)L(\lambda)]$, with $L(\lambda)$ a Lorentzian function of maximum value unity, centred at λ_r. We note that using Eq. (3) instead of Eq. (1) is not really needed for analysis of a single dip. However, we already introduce Eq. (3) since it simplifies the integration in Appendix A.

A fit of Eq. (3) to the measured dip of Fig. 2(b) yields the blue curve in that figure, giving fit parameters $\varepsilon = 0.043$ and $\gamma_r = 122$ pm. Thus, the quality factor $Q = \lambda_r/\gamma_r$ is 12706. The value of ε being close to zero, the ring operates close to critical coupling, which holds for [15] $a = 1$, *i.e.* $\varepsilon = 0$. With $n_g = 4.37$ derived from the free spectral range $P_{\text{RR}} = \lambda_r^2/(n_g L) = 6.01$ nm, Eqs. (4,5) give the values $r = 0.975$ and $a = 0.987$.

3. Fiber interrogator

3.1. Circuitry and signal flow of the interrogator

The interrogator is a fiber optic circuit based on a Mach-Zehnder interferometer (MZI) with a 2×2 input coupler and a 3×3 output coupler. The circuit is depicted in Fig. 3. Light from a broadband source (BBS, EXALOS EXS210069-01 superluminescent diode, maximum output power 14 mW) is guided to the sensor, via a circulator, a fiber Bragg grating (FBG, from TeraXion, FWHM 200 pm) and an EDFA set at gain of 24 dB (Amonics, AEDFA-PM-33-B-FA). The width of the FBG reflection spectrum is such that a single dip can be selected by tuning the center of the FBG spectrum to the sensor's resonance wavelength in the absence of ultrasound, by applying strain. The light from the sensor is guided to the MZI, of which one arm has a variable length air gap, realized using two lenses (ThorLabs FiberPort collimators), one of which is translatable. Thus, a variable optical path difference (OPD) is provided. One input of the 3×3 coupler is left open. Outputs are connected to a combination of a photodetector (Fermionics, FD100) and a transimpedance amplifier (TIA, ADA4899-1 from Analog Devices with gain 2.2 kV/A), after which further amplification (gain=196) is applied (not shown in Fig. 3). The resulting output voltages V_i are sampled by a data acquisition system (based on National Instruments NI 5734,

Optics EXPRESS

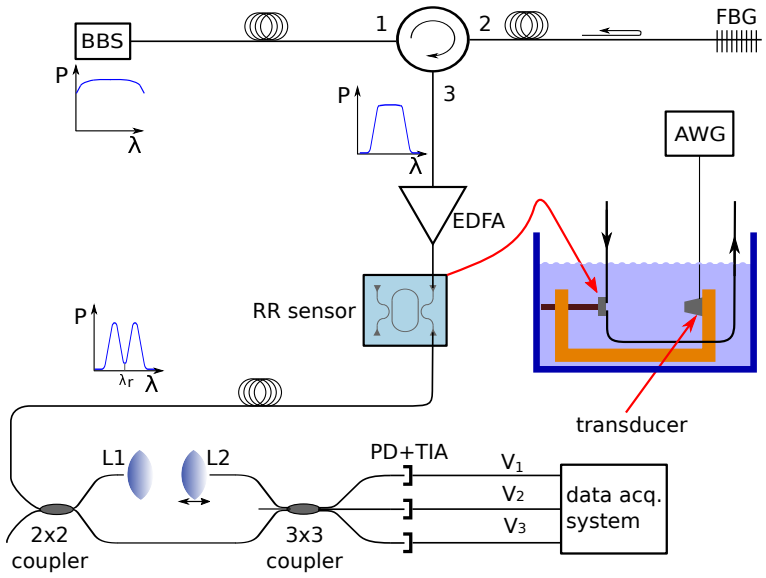

Fig. 3. Schematic of the fiber interrogator, based on a Mach-Zehnder interferometer with a 2×2 coupler and a 3×3 coupler. BBS is the broadband source, FBG the fiber Bragg grating, EDFA the erbium doped amplifier and AWG the arbitrary waveform generator. Sensor #1 is placed at 135 mm from the transducer and sensor #2 is placed at 149 mm. The lenses L1 and L2 are part of the variable optical path length of one MZI arm, ranging from 4 to 13.5 mm. PD + TIA denotes combination of photodetector and transimpedance amplifier. V_1, V_2 and V_3 are the three output voltages used to calculate the orthogonal voltages V_x and V_y and the angular deflection $\Phi(t)$ (see section 4.1). The signal spectrum has been indicated at the BBS, after the circulator and before the MZI. The water tank with sensor and transducer shows the setup for ultrasound measurements.

max. sampling rate 120 MSa/s, high pass filtering with cutoff frequency at $f_c = 20.0$ kHz). The sensor is immersed in a water tank, mounted on one side of a frame (see Fig. 3). On the other side, actuated by an arbitrary waveform generator (AWG, Rigol DG1022), a transducer is mounted for sending ultrasound waves. Prior to ultrasound measurements with the sensor, the ultrasound pressure is calibrated with a hydrophone (Precision Acoustics, SN2082, 1.0 mm) placed at the sensor's position.

The power transmission T_i ($i = 1, 2, 3$) of the MZI, supposed lossless, at the optical outputs is given by [16]

$$T_{\mathrm{MZI},i} = \frac{1}{3}\left[p + q\cos\left(\frac{2\pi}{\lambda}\mathrm{OPD} + \varphi_i + \varphi_e\right)\right] \approx \frac{1}{3}\left[p + q\cos\left(\xi\lambda + \varphi_i + \psi_e\right)\right]. \tag{6}$$

The parameters p and q determine the fringe visibility q/p. OPD is the aforementioned optical path difference. For an ideal 3×3 coupler $p = 1$ and $\varphi_i = 0°, 120°, -120°$ for $i = 1, 2, 3$. The phase φ_e is a so-called environmental phase [9], that drifts slowly in time. Its origin is temperature instability of the fiber optic circuit. Owing to the three phase shifted cosines in Eq. (6), at least two of the voltages V_i are non-zero for any argument of the cosines, thus avoiding signal fading [9]. The right side of Eq. (6) is obtained by Taylor expanding $1/\lambda$ in the argument of the cosine around $\lambda = \lambda_r$. Here we only retained the first order term, as the deviation of λ from λ_r is about 100 pm, to be compared with $\lambda_r \cong 1550$ nm. We have used $\xi = 2\pi\mathrm{OPD}/\lambda_r^2 = 2\pi/\mathrm{FSR}$, with FSR the MZI's free spectral range. Further, ψ_e is defined by $\psi_e = -4\pi\mathrm{OPD}/\lambda_r - \varphi_e$, which thus shows the same drift as φ_e. Renumbering the outputs has removed the minus sign of φ_i. $T_{\mathrm{MZI},i}$ of

Optics EXPRESS

Eq. (6) is a main ingredient in deriving output voltages V_i (see Appendix A).

3.2. Characterization of the fiber Bragg grating and Mach-Zehnder interferometer

The FBG was characterized by measuring its reflection spectrum, using an optical spectrum analyzer (OSA, Yokogawa AQ6315A) coupled to port 3 of the circulator (see Fig. 3). Figure 4(a) shows the spectrum (blue data points), which has a top-hat shape and decays steeply. We have fitted a super-Lorentzian function to the data points. This function is given by [17]

$$R_{\mathrm{FBG}}(\lambda) = \left[1 + \left(\frac{\lambda - \lambda_0}{\gamma_{\mathrm{FBG}}/2}\right)^N\right]^{-1}. \tag{7}$$

Here γ_{FBG} is the FWHM, λ_0 the central wavelength, and the integer N the order of the super-Lorentzian. $N = 8$ gives the best fit result. In Fig. 4(a) we also show the fitted function, which yields $\gamma_{\mathrm{FBG}} = 207$ pm, in agreement with the specification.

The combined spectrum of the FBG and sensor #1 is presented in Fig. 4(a) as well (green data points). It was measured in the configuration of Fig. 3, but with the difference that the OSA instead of the MZI is coupled to the sensor's pass port. Alignment of the FBG spectrum is close to symmetric with respect to the resonance dip, which here is broader than in Fig. 2(b), as a result of the limited resolution of the OSA. The small blue shift of the resonance wavelength is attributed to a slightly lower device temperature. The combined spectrum indicates a latitude of about 100 pm before the dip moves out of the FBG spectrum as a result of applied ultrasound.

The MZI was characterized by directly connecting a tunable laser (Santec TSL-210VF, set at output power 500 μW) to the MZI input, to measure the output voltages V_i as a function of wavelength. The wavelength was swept from 1550 to 1551 nm at a rate of 1.2 nm/min, giving a measurement time of 50 s. This time, unlike the very short measurement times in the ultrasound experiments (section 4.2), is comparable to the time scale of the environmental phase drift. Therefore, a stabilization time of the setup of several hours was observed before this characterization, with the laser on. The characterization was done for five OPDs, *i.e.* five positions of lens L2 in Fig. 3. In agreement with Eq. (7), the resulting five sets of $V_i(\lambda)$ traces are cosines, each oscillating around a non-zero average.

Traces for OPD = 12.9 mm are shown in Fig. 4(b), together with fits of the function $V_i = A_i \cos(\xi\lambda + \varphi_i + \psi_e)$ to the traces, from which first the average was subtracted. The fits are performed for the five sets, treating A_i and the sum $\varphi_i + \psi_e$ as fit parameters. The fits indicate that the amplitudes of the three cosines of a set are not equal (see caption), which contradicts Eq. (7). This implies that the circle defined by voltages V_x and V_y in Eqs. (A17) and (A18), respectively, is deformed to an ellipse. As explained in Appendix A, the circular shape defined by these equations plays a central role in the interrogation procedure. Taking for the traces of Fig. 4(b) the fitted phase of output V_1 as a reference ($\varphi_1 + \psi_e = 0$), we obtain $\varphi_2 + \psi_e = -117°$ and $\varphi_3 + \psi_e = 117°$. Thus, the phases deviate somewhat from the nominal values. We note that slight non-ideal behavior of amplitude and phase of 3×3 fiber couplers is not uncommon and has been reported before [8, 18].

In order to make the amplitudes of the cosines equal, we modified Eqs. (A17) and (A18) by including correction factors c_2 and c_3:

$$V_x = 2V_1 - c_2V_2 - c_3V_3 \tag{8}$$

$$V_y = \sqrt{3}\,(c_3V_3 - c_2V_2)\,. \tag{9}$$

Initially, we set $c_2 = c_3 = 1$ for the traces in Fig. 4(b). Using these start values, the equation of the ellipse given by the locus of points (V_x, V_y) defined by Eqs. (8) and (9) is obtained by least square fitting [19], giving the ellipse semi-axes a and b. Next, the function $f(c_2, c_3) =$

Optics EXPRESS

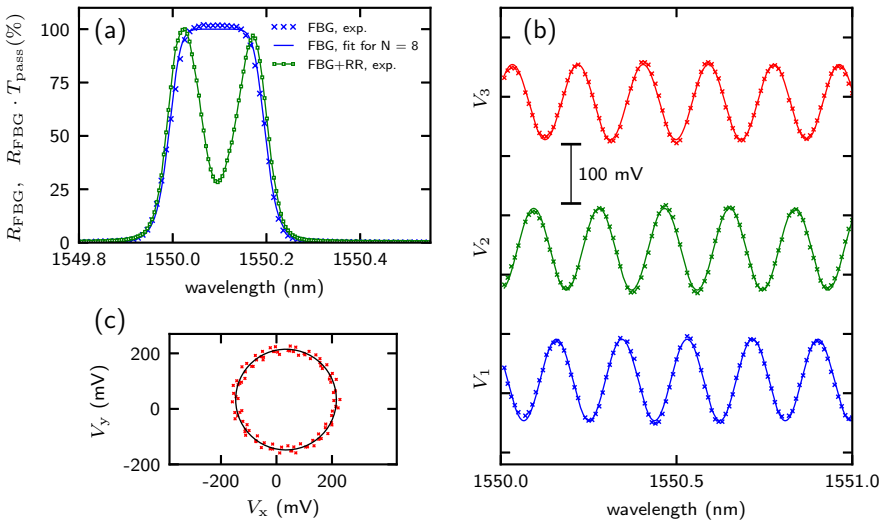

Fig. 4. (a) FBG reflection spectrum and combined FBG reflection and RR transmission spectrum, both normalized to their maximum value, and a fit of Eq. (7) to the FBG spectrum for $N = 8$. (b) Traces of the interrogator outputs V_i as a function of wavelength, with data points shown as crosses. Due to the way of plotting, the DC component of the V_i is not visible. The oscillatory functions are fits of $A_i \cos(\xi\lambda + \varphi_i + \psi_e)$ to the data points. The fits give: A_i = 63.4, 68.9 and 68.7 mV ($i = 1, 2, 3$) and $\varphi_i + \psi_e$ = 176°, 59° and -67° (i = 1,2,3). The traces were used in obtaining the correction factors and in Eqs. (9) and (10). (c) Corrected (V_x, V_y) points, together with the fitted circle. The circle radius is 181 mV.

$|1 - a(c_2, c_3)/b(c_2, c_3)|$ is minimized [20], yielding the circle aimed for. The result is $c_2 = 0.85$ and $c_3 = 0.86$, for minimum $f(c_2, c_3) = 0.001$. The corrected (V_x, V_y) points have been plotted in Fig. 4(c), together with the fitted circle. The correction factors c_2 and c_3 are used in the interrogation procedure of section 4.2.

4. Interrogation of the ultrasound sensor

4.1. Interrogation procedure

The goal of the interrogation procedure is quantitative extraction of the ultrasound-induced optical signal of the sensor from the output voltages $V_i(t)$. Appendix A is the basis of the procedure. Here, we give the main data-processing steps for continuous wave ultrasound of frequency f_0. We start from slightly modified versions of Eqs. (A20) and (A21) for the mutual orthogonal voltages $V_x(t)$ and $V_y(t)$ constructed from the measured $V_i(t)$:

$$V_x(t) = 2V_1(t) - V_2(t) - V_3(t) = 3R_K \cos(\Phi(t) + \psi_e) + x_0(\psi_e) \tag{10}$$

$$V_y(t) = \sqrt{3}\,(V_3(t) - V_2(t)) = 3R_K \sin(\Phi(t) + \psi_e) + y_0(\psi_e). \tag{11}$$

The modifications comprise neglect of constant parameters in the argument of the cosine and sine, and in the functions x_0 and y_0, which are understood to be absorbed in ψ_e. This simplifies the analysis, but has no consequences for the final result. Eqs. (10) and (11) are parametric equations of a circle of radius $3R_K$ and with center (x_0, y_0). $\Phi(t) = \Phi_0 \sin(2\pi f_0 t)$ is the instantaneous angular deflection of the point (V_x, V_y) on an arc of the circle, which is periodically traced at the

Optics EXPRESS

frequency f_0. R_K is constant for constant total gain of the interrogator circuit, independent of the applied ultrasound pressure, but dependent on the MZI's OPD. Dependence of $V_x(t)$ and $V_y(t)$ on the environmental phase ψ_e is not an issue, since ψ_e is constant on the time scale of a single interrogation of the sensor.

The data-processing steps are as follows. First, for a high enough reference pressure, the radius $3R_K$ and the center (x_0, y_0) are determined using the fit procedure already described for an ellipse in section 3.2. The fitted value of $3R_K$ then holds for all other pressures of a measurement series. For a series, we typically use a rather high reference pressure, since a high pressure gives a long arc and thus an accurate fit result for $3R_K$.

Next, the fitted $3R_K$ is used to retrieve the circle center (x_0, y_0) for each pressure amplitude p_0 of the series by minimizing [19, 20] the average squared deviations of the locus of points (V_x, V_y) from a circle of radius $3R_K$.

Subsequently, for each pressure of the series we determine the instantaneous deflection. In more detail, we obtain the wrapped deflection from Eqs. (10) and (11) according to

$$\Phi(t)_{\mathrm{wr.}} = \mathrm{atan2}\left(V_y - \mathrm{y}_0, V_x - \mathrm{x}_0\right) - \psi_{\mathrm{e}}. \tag{12}$$

Here atan2 is the four-quadrant arctangent function. Upon input of the coordinates of a point in the plane, atan2 returns the angle of the point in the range $(-\pi, \pi]$. $\Phi(t)_{\mathrm{wr.}}$ in principle oscillates regularly in time around $-\psi_e$, but may be discontinuous in view of the limited range of atan2. Therefore, we unwrap $\Phi(t)_{\mathrm{wr.}}$ using the unwrap function of MATLAB [21], which returns the smooth unwrapped deflection. After subtracting from the unwrapped deflection its average $-\psi_e$, we arrive at the proper instantaneous deflection $\Phi(t)$, which describes the periodic tracing of the circle arc. Fourier transformation of $\Phi(t)$ then yields the amplitude Φ_0, the quantity sought for.

In the last step, again following Appendix A, the amplitude δ_0 of the resonance-wavelength modulation is obtained from

$$\delta_0 = \kappa \frac{\Phi_0}{\xi} = \kappa \frac{\lambda_r^2 \Phi_0}{2\pi \mathrm{OPD}}. \tag{13}$$

Here κ is the correction factor introduced in Appendix A. However, instead of obtaining δ_0, we will use this equation in the next section to make an experimental test of the value of κ.

The data-processing just described is performed offline, which is adequate for the present purpose. Various scenarios can be conceived for real-time data processing, which is required for later application to IVUS imaging.

4.2. Interrogation experiments

We interrogated sensors #1 and #2 according to the above procedure, using OPD values of 6.9 and 12.9 mm, which almost span the available range. We applied two series of pressures amplitudes, which become apparent in Fig. 6 below. For each pressure we acquired time traces of the three voltages $V_i(t)$ during 300 ms, sampled at 30 MSa/s.

In Fig. 5(a), as an example, we show for sensor #1 part of the $V_i(t)$ traces and of the $V_x(t)$ and $V_y(t)$ traces deduced from these, for OPD = 12.9 mm and a pressure of 2280 Pa, the reference pressure for determining radius $3R_K$ for this sensor. Similar traces (not shown) were obtained for sensor #2 for reference pressure 312 Pa. The traces results after noise reduction, applying a Gaussian bandpass filter of FWHM = 80 Hz centred at the fundamental frequency and its harmonics. The ultrasound period of 0.77 μs is clearly present in the traces, while the second harmonic can be seen as well. In Fig. 5(b) the points (V_x, V_y) are plotted, together with the fitted circle of radius $3R_K$ = (191± 6) mV. The spectral content of the $V_i(t)$ of sensor #1 is more apparent in the Fourier transforms in Fig. 5(c), in which the transforms for sensor #2 are included as well for reference pressure 312 Pa. Apart from the fundamental frequency (1.3 and 0.77 MHz for sensor #1 and #2, respectively), the transforms also show peaks for the second and third harmonic, albeit a very small peak for the third harmonic. Peaks at the harmonics agree with the

Optics EXPRESS

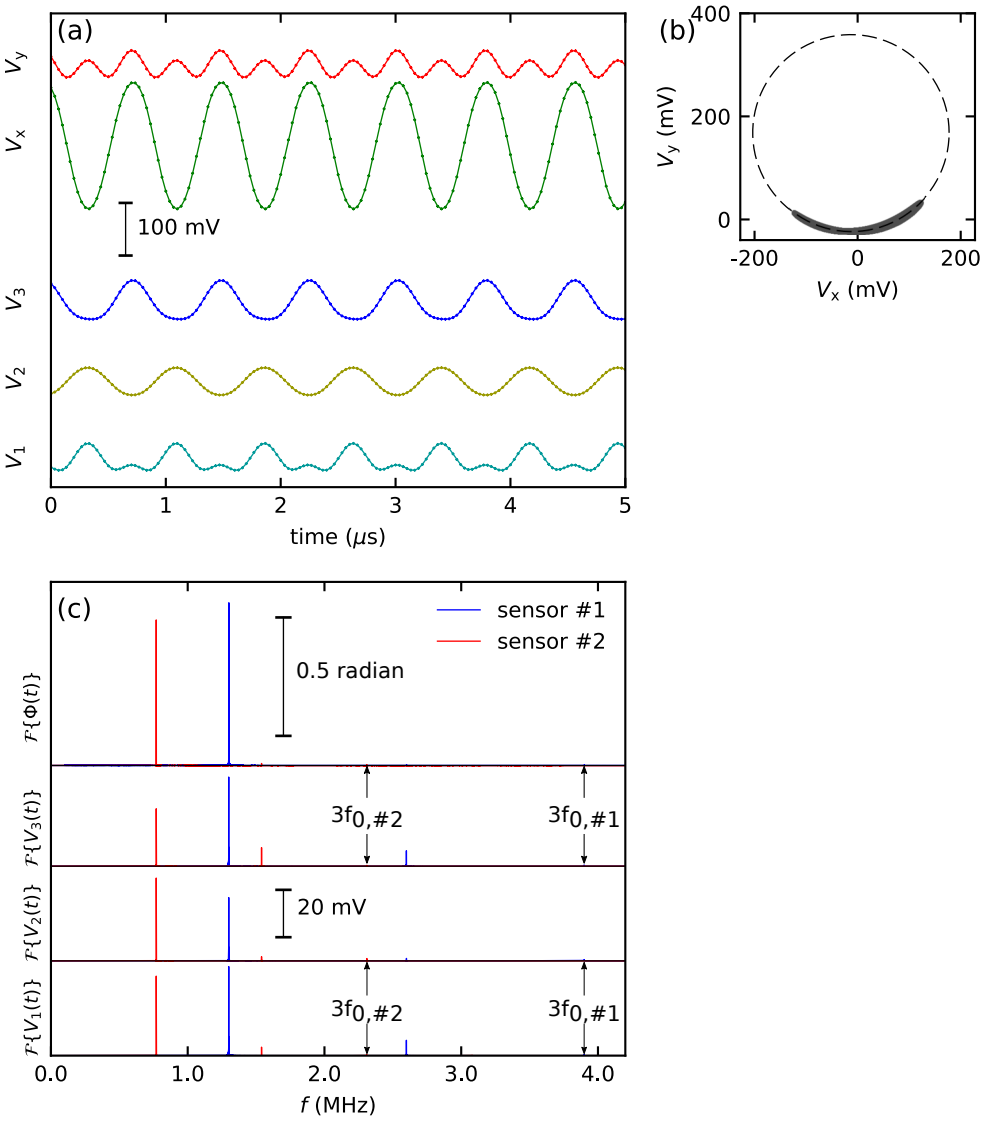

Fig. 5. (a) Part of traces of $V_i(t)$ $(i = 1, 2, 3)$ for sensor #1, sampled while interrogating the sensor, and of the mutual orthogonal voltages V_x and V_y, for OPD = 12.9 mm and p_0 = 2280 Pa. (b) Plot of the points (V_x, V_y), which trace a circle arc, together with the fitted circle. (c) Fourier transforms of the $V_i(t)$ and of the angular deflection $\Phi(t)$ for OPD = 12.9 mm and p_0 = 2280 Pa (sensor #1) and p_0 = 312 Pa (sensor #2). The weak signals at the third harmonic are indicated as $3f_{0,\#1}$ and $3f_{0,\#2}$ for sensor #1 and #2, respectively.

Optics EXPRESS

Bessel function expansion referred to in Appendix A. To obtain the angular deflection $\Phi(t)$ we follow section 4.1, leading to the Fourier transforms in Fig. 5(c), upper panel. At the fundamental frequency the transforms show a sharp peak. Its height is the angular deflection's amplitude and amounts to Φ_0 = (0.69 ±0.04) radian and Φ_0 = (0.62±0.05) radian for sensor #1 and #2, respectively. This is the main interrogation result for these experimental conditions.

For all other pressures we determined the $\Phi(t)$ traces and the corresponding amplitudes Φ_0 for both sensors. For sensor #1, Fig. 6(a) shows the main plot of Φ_0 versus p_0. The pressure range is 2.3 - 5750 Pa. Figure 6(b) zooms in on the lower pressures. The straight lines through the origin are fits to those data points showing the linear behavior discussed in Appendix A. The slopes $\partial\Phi_0/\partial p_0$ of the fitted lines, which are the sensitivities of sensor #1 for these OPDs, are given in Table 1, along with the sensitivities of sensor #2 and other parameters of the two sensors. For sensor #2, a comparable data set is shown in Fig. 6(c,d) for the pressure range 1.2 - 775 Pa. The plots indicate that sensor #2 is more sensitive than sensor #1. This arises from the larger membrane diameter of sensor #1, which results in a larger membrane deflection per unit of pressure. Further, the sensitivity is higher for the larger OPD for both devices. This agrees with Eq. (13), which indicates that the ratio Φ_0/OPD is constant for a constant δ_0. The sub-linear behavior in the plots above a certain pressure indicates that in that range the amplitude of the resonance-wavelength modulation is such that the bandwidth of the FBG becomes limiting. The minimum pressures we succeed to detect in these measurements are 2.3 and 1.2 Pa for sensor #1 and #2, respectively, detection limits comparable to the one reported in [7]. The present detection limit is determined by sources of disturbing signal external to the interrogator. For optimum electromagnetic shielding, the combined noise of the photodetectors and their amplifiers and the noise of the broadband light source will be limiting for the signal-to-noise ratio of the interrogator

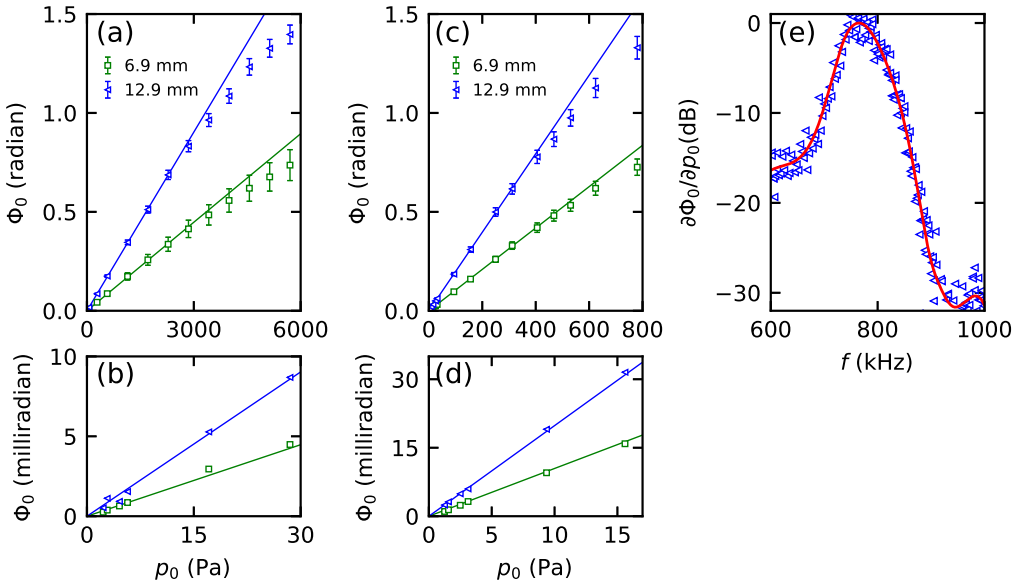

Fig. 6. Main results of the interrogation of the sensors: (a) amplitude of the angular deflection Φ_0 for sensor #1 as a function of the pressure amplitude p_0 of 1.3 MHz ultrasound. (b) Zoom-in of (a) for the pressure range 0-30 Pa. (c) Amplitude of the angular deflection Φ_0 for sensor #2 as a function of the pressure amplitude p_0 of 0.77 MHz ultrasound. (d) Zoom-in of (c) for the pressure range 0-15 Pa. In (a)-(d) OPDs of the MZI are as stated and the lines are fitted straight lines through the origin. (e) Sensitivity as a function of frequency of sensor #2 for OPD = 12.9 mm.

Optics EXPRESS

Table 1. Parameters obtained for sensors #1 and #2: $\partial\Phi_0/\partial p_0$ is the sensor sensitivity, $\partial\delta_0/\partial p_0$ is the amplitude of the resonance-wavelength modulation of the sensor per unit of pressure, while $\kappa_{\text{exp.}}$ and $\kappa_{\text{theo.}}$ are the experimental and theoretical correction factors, respectively, which relate to Eq.(13). The uncertainty in $\partial\delta_0/\partial p_0$ was omitted, since its contribution to the uncertainty of $\kappa_{\text{exp.}}$ is negligible.

OPD (mm)	Parameter	Sensor #1	Sensor #2
6.9	$\partial\Phi_0/\partial p_0$	0.15 ± 0.02	1.04 ± 0.06
12.9	(milliradian/Pa)	0.30 ± 0.01	1.98 ± 0.08
-	$\partial\delta_0/\partial p_0$ (fm/Pa)	21.4	103.8
6.9	$\kappa_{\text{exp.}}$	2.6 ± 0.3	1.8 ± 0.1
12.9		2.41 ± 0.08	1.77 ± 0.07
6.9	$\kappa_{\text{theo.}}$	1.07	1.03
12.9		1.26	1.16

outputs.

The data shown in Fig. 6(a)-(d) were obtained using monochromatic continuous wave ultrasound, chosen at the frequency of the membrane's maximum deflection. The sensors, however, are broadband owing to the membrane's intrinsic loss. This property is apparent from the sensitivity as a function of frequency, which for sensor #2 is shown in Fig. 6(e). The function plotted is $\partial\Phi_0/\partial p_0$, normalized to unity at its maximum. It was measured using continuous waves and a frequency sweep. The function has the typical shape for a damped resonator. The peak occurs at 0.77 MHz, while the -6 dB bandwidth is 14.5%. This sensitivity curve and the one in [7] for the same sensor are very close to each other. We note that the bandwidth of the sensor enables application of tailored ultrasound pulses, as may be more appropriate for later imaging. If for certain applications a larger bandwidth is needed, it can for example be increased by adding a lossy layer to the membrane.

We now discuss the correction factor κ occurring in Eq. (13) and finally, in relation to κ, make further comments on the sensitivities $\partial\Phi_0/\partial p_0$ listed in Table 1. From Eq. (13), the correction factor can be rewritten as $\kappa = 2\pi\text{OPD}(\partial\delta_0/\partial\text{p}_0)/(\lambda_r^2(\partial\Phi_0/\partial\text{p}_0))$, where the missing ingredient is $\partial\delta_0/\partial p_0$. The pressure dependence of δ_0 is derived using the modulation method detailed in Appendix B, for low pressures leading to linear behavior and the derivatives $\partial\Phi_0/\partial p_0$ listed in Table 1. For the two sensors and for either OPD we thus obtain the experimental values $\kappa_{\text{exp.}}$ listed in Table 1, to be compared with the listed values $\kappa_{\text{theo.}}$ taken from Appendix A (discussed there in relation to Fig. A1). The $\kappa_{\text{exp.}}$ values for sensor #1 exceed those of sensor #2, in agreement with the behaviour of $\kappa_{\text{theo.}}$. Further, on average the ratio of the values is 0.47 for sensor #1 and 0.61 for sensor #2. In our opinion, the agreement to much better than one order of magnitude validates the mathematical description of Appendix A in presenting the proper physics picture.

The ratio of the experimental sensitivities in Table 1 for the two OPDs equals 0.50 and 0.53 for sensor #1 and sensor #2, respectively. The ratio of the theoretical sensitivities can be obtained using the above relation between κ and $\partial\Phi_0/\partial p_0$ (where we use $\kappa_{\text{theo.}}$). This yields for the theoretical ratio 0.63 and 0.60 for sensor #1 and sensor #2, respectively. The relative difference between the theoretical and experimental sensitivity ratios is 18% on average. This indicates a high degree of consistency of our description of the operation of the interrogator and the actual interrogation experiments.

Optics EXPRESS

Conclusion and outlook

We interrogated two silicon ring-resonator sensors for ultrasound in the MHz range using an interrogator based on a fiber Mach-Zehnder interferometer (MZI), by applying the procedure based on our mathematical description of the interrogator operation in Appendix A. According to the geometrical interpretation of the operation, the amplitude of the angular deflection Φ_0 on the circle arc periodically traced in the plane of the two orthogonal interrogator voltages, is the principal sensor signal. Φ_0 is proportional to the amplitude of the resonance-wavelength modulation of the sensor in response to the ultrasound. The main interrogation results are the linear relations between Φ_0 and the pressure amplitude of continuous wave ultrasound, in a broad pressure range and for optical path differences (OPDs) of the MZI of 6.9 and 12.9 mm. The minimum detected pressures is 1.2 Pa. For sensor #1, the sensitivity amounts to 0.15 and 0.30 milliradian/Pa, for OPDs of 6.9 and 12.9 mm, respectively. For sensor #2, the sensitivity is 1.04 and 1.98 milliradian/Pa for these OPDs. This higher sensitivity for the larger OPD is accompanied by a lower output voltages of the MZI, in agreement with the prediction in Appendix A. This suggests a trade-off between sensitivity and signal strength, for which in future a brighter broadband source will be helpful, also for avoiding the EDFA we use now. Using an independent method of calibrating the optical response of the sensor to ultrasound, we arrive at a resonance-wavelength modulation per unit of pressure of 21.4 fm/Pa (sensor #1) and 103.8 fm/Pa (sensor #2).

This work on the fiber interrogator is an important step towards an integrated photonics interrogator, which is our next goal. The architecture of an integrated photonics version can be similar to that of the fiber version. An integrated photonics version, however, will be much smaller, implying that its temperature can be easily stabilized, such that the environmental phase drift we have encountered here will be strongly reduced. An integrated photonics version can be designed for interrogating an array of integrated ultrasound sensors for IVUS by applying multiplexing using arrayed waveguide gratings, a certain version of which we have already implemented for the multiplexing of FBG sensors [22]. The ultrasound sensors will then be equipped with a drop port, which gives a peak in the transmission resembling the reflected peak of FBG sensors considered in [22].

Appendix A : Mathematical description of the operation of the fiber interrogator

In this Appendix we present a mathematical description of the operation of the fiber interrogator when interrogating a ring-resonator sensor in the pass-port configuration. Based on the overall signal flow we arrive at the three outputs of the MZI, of which specific linear combinations yield the signal that is a measure of the amplitude of the applied ultrasound waves. The interrogation procedure we follow in the main text is based on this Appendix. Reproducing Eqs. (3), (6) and (7) of the main text, the latter for $N = 8$ and $\lambda_0 = \lambda_r$, gives

$$T_{\text{pass}}(\lambda, \widetilde{\delta\lambda_r}) = \frac{\left(\lambda - \lambda_r - \widetilde{\delta\lambda_r}(t)\right)^2 + \varepsilon(\gamma_r/2)^2}{\left(\lambda - \lambda_r - \widetilde{\delta\lambda_r}(t)\right)^2 + (\gamma_r/2)^2} \tag{A1}$$

$$T_{\text{MZI},i}(\lambda) = \frac{1}{3}\left[p + q\cos\left(\xi\lambda + \varphi_i + \psi_e\right)\right] \tag{A2}$$

$$\text{with } \varphi_i = 0°, 120°, -120° \text{ for } i = 1, 2, 3.$$

$$R_{\text{FBG}}(\lambda) = \frac{1}{1 + \left(\frac{\lambda - \lambda_r}{\gamma_{\text{FBG}}/2}\right)^8}. \tag{A3}$$

Optics EXPRESS

Eq. (A1) includes the resonance-wavelength modulation $\widetilde{\delta\lambda_r} \equiv \widetilde{\delta\lambda_r}(t) = \delta_0 \sin(2\pi f_0 t)$ resulting from application of ultrasound waves of frequency f_0 . Following the signal path in Fig. 3 and using the integrating property of the photodetectors, we can write the time-dependent output voltage of the TIAs as

$$V_i(\widetilde{\delta\lambda_r}) = \alpha P_{\mathrm{BBS}} R_{\mathrm{ph}} G \int_0^\infty R_{\mathrm{FBG}}(\lambda) T_{\mathrm{pass}}(\lambda, \widetilde{\delta\lambda_r}) T_{\mathrm{MZI},i}(\lambda) d\lambda. \tag{A4}$$

Here P_{BBS} is the power density of the broadband source, supposed constant in the range the FBG spectrum. R_{ph} is the responsivity of the photodetectors, G the combined gain of the EDFA and TIA, while α is a transmission coefficient of the overall fiber optic circuit. In the following we drop the prefactors of the integral, since these turn out to cancel when extracting Φ_0, which is the principal sensor signal defined below. Also dropping the factor 1/3 of $T_{\mathrm{MZI},i}$ and the subscripts FBG and pass, this leads to $I_i(\widetilde{\delta\lambda_r})$, the i^{th} component of the integral proportional to the voltage $V_i(\widetilde{\delta\lambda_r})$

$$\begin{aligned} I_i &= \int_0^\infty R(\lambda) T(\lambda, \widetilde{\delta\lambda_r}) \left[p + q\cos\left(\xi\lambda + \varphi_i + \psi_e\right)\right] \mathrm{d}\lambda \\ &= p\int_0^\infty R(\lambda) T(\lambda, \widetilde{\delta\lambda_r}) \mathrm{d}\lambda + q\int_0^\infty R(\lambda) T(\lambda, \widetilde{\delta\lambda_r}) \cos\left(\xi\lambda + \varphi_i + \psi_e\right) \mathrm{d}\lambda \\ &= p I_\alpha(\widetilde{\delta\lambda_r}) + q I_{\beta,i}(\widetilde{\delta\lambda_r}). \end{aligned} \tag{A5}$$

Here we have used

$$I_\alpha(\widetilde{\delta\lambda_r}) = \int_0^\infty R(\lambda) T(\lambda, \widetilde{\delta\lambda_r}) d\lambda \tag{A6}$$

$$\begin{aligned} I_{\beta,i}(\widetilde{\delta\lambda_r}) &= \int_0^\infty R(\lambda) T(\lambda, \widetilde{\delta\lambda_r}) \cos(\xi\lambda + \varphi_i + \psi_e) d\lambda \\ &= \mathrm{Re}\left\{ e^{i(\varphi_i + \psi_e)} \int_0^{+\infty} R(\lambda) T(\lambda, \widetilde{\delta\lambda_r}) e^{i\xi\lambda} d\lambda \right\}. \end{aligned} \tag{A7}$$

By substituting the expressions for $T(\lambda, \widetilde{\delta\lambda_r})$ and $R(\lambda)$ from Eqs. (A1) and (A3) into Eqs. (A6) and (A7), we obtain

$$\hat{J} \equiv \int_0^\infty R(\lambda) T(\lambda, \widetilde{\delta\lambda_r}) e^{i\xi\lambda} d\lambda = \int_0^\infty \frac{\left(\lambda - \lambda_r - \widetilde{\delta\lambda_r}\right)^2 + \varepsilon(\gamma_r/2)^2}{\left(\lambda - \lambda_r - \widetilde{\delta\lambda_r}\right)^2 + (\gamma_r/2)^2} \frac{e^{i\xi\lambda}}{1 + \left(\frac{\lambda - \lambda_r}{\gamma_{\mathrm{FBG}}/2}\right)^8} d\lambda. \tag{A8}$$

The integrals $I_\alpha(t)$ and $I_{\beta,i}(t)$ can then be written as

$$I_\alpha(t) = \hat{J}\big|_{\xi=0} \tag{A9}$$

$$I_{\beta,i}(t) = \mathrm{Re}\left\{ e^{i(\varphi_i + \psi_e)} \hat{J} \right\}. \tag{A10}$$

Since the integrand in Eq. (A8) is vanishingly small for $\lambda \leq 0$, the lower value of the integration interval can be taken as $-\infty$. Making the substitution $\lambda - \lambda_r \rightarrow z$ in Eq. (A8) and using contour integration we obtain

$$\hat{J}/e^{i\xi\lambda_r} \equiv \hat{K} = \oint_C \frac{\left(z - \widetilde{\delta\lambda_r}\right)^2 + \varepsilon(\gamma_r/2)^2}{\left(z - \widetilde{\delta\lambda_r}\right)^2 + (\gamma_r/2)^2} \frac{e^{i\xi z}}{1 + \left(\frac{z}{\gamma_{\mathrm{FBG}}/2}\right)^8} dz = \oint_C f(z) dz. \tag{A11}$$

The contour C is the upper half circle of radius R in the complex plane, including the interval $[-R, R]$ of the real axis, taken in the limit $R \to \infty$. The poles of $f(z)$ arise from the RR transmission function and FBG reflection function, respectively, and for the contour C occur for $z_{\mathrm{RR}} = \widetilde{\delta\lambda_r} + i\gamma_r/2$ (RR pole) and $z_{\mathrm{FBG,k}} = \left(\gamma_{\mathrm{FBG}}/2\right) \exp\left[i\pi\left(k + 1/2\right)/4\right]$, $k = 0, 1, 2, 3$ (FBG poles). Using Cauchy's residue theorem, the integral is evaluated to obtain

$$\oint_C f(z)dz = \hat{F}(\widetilde{\delta\lambda_r}) + \hat{G}(\widetilde{\delta\lambda_r}). \tag{A12}$$

Here $\hat{F}(\widetilde{\delta\lambda_r})$ and $\hat{G}(\widetilde{\delta\lambda_r})$ are given by:

$$\hat{F}(\widetilde{\delta\lambda_r}) = -\frac{\pi\gamma_r}{2} \frac{(1-\varepsilon)\, e^{-\xi\gamma_r/2}}{1 + \left(\frac{\widetilde{\delta\lambda_r} + i\gamma_r/2}{\gamma_{\mathrm{FBG}}/2}\right)^8} e^{i\xi\widetilde{\delta\lambda_r}} \equiv \hat{E}(\widetilde{\delta\lambda_r}) e^{i\xi\widetilde{\delta\lambda_r}} \tag{A13}$$

$$\hat{G}(\widetilde{\delta\lambda_r}) = -i\frac{\pi}{4} \sum_{k=0}^{3} \frac{z_{\mathrm{FBG,k}} \left[\left(z_{\mathrm{FBG,k}} - \widetilde{\delta\lambda_r}\right)^2 + \varepsilon(\gamma_r/2)^2\right]}{\left(z_{\mathrm{FBG,k}} - \widetilde{\delta\lambda_r}\right)^2 + (\gamma_r/2)^2} e^{i\xi \mathrm{Re}\left(z_{\mathrm{FBG,k}}\right)} e^{-\xi \mathrm{Im}\left(z_{\mathrm{FBG,k}}\right)}. \tag{A14}$$

The complex functions $\hat{F}(\widetilde{\delta\lambda_r})$ and $\hat{G}(\widetilde{\delta\lambda_r})$ are time-domain (oscillatory) signals resulting from light interference in the 3×3 coupler, the time dependence being expressed by $\widetilde{\delta\lambda_r}(t)$.

The oscillatory behavior of $\hat{F}(\widetilde{\delta\lambda_r})$ is recognized to the full extent from the Bessel function expansions [23] of $\exp(i\xi\widetilde{\delta\lambda_r}) = \cos\left[\xi\lambda\delta_0 \sin(2\pi f_0 t)\right] + i \sin\left[\xi\lambda\delta_0 \sin(2\pi f_0 t)\right]$, which apart from terms at the fundamental frequency also give harmonics. The factor $\exp(i\xi\widetilde{\delta\lambda_r})$ is multiplied by the envelope $\hat{E}(\widetilde{\delta\lambda_r})$, implicitly defined in Eq. (A13). The envelope includes both RR and FBG parameters and attenuates the oscillations with increasing δ_0 and increasing OPD. This OPD-dependence follows from the damping factor $\exp(-\xi\gamma_r/2) = \exp(-\mathrm{OPD}/L_{c,r})$. Here $L_{c,r}$ is the coherence length related to the spectral width of the ring's resonance dip. $L_{c,r}$ limits the OPDs of the MZI for which fringes in traces $V_i(t)$ can be resolved experimentally. For the resonances we use for the sensing, $L_{c,r}$ is in the range 6 - 8 mm.

$\hat{G}(\widetilde{\delta\lambda_r})$ arises from interference of waves within the bandwidth of the FBG, each FBG pole giving rise its own interference signal, damped by the factor $\exp\left[-\xi \mathrm{Im}\left(z_{\mathrm{FBG,k}}\right)\right] = \exp\left(-\mathrm{OPD}/L^k_{\mathrm{c,FBG}}\right)$. Here $L^k_{\mathrm{c,FBG}}$ is the coherence length related to the width of the FBG spectrum and due to the k^{th} FBG pole. It is given by

$$L^k_{\mathrm{c,FBG}} = \frac{\lambda_r^2}{2\pi \mathrm{Im}(z_{\mathrm{FBG,k}})} = \frac{\lambda_r^2}{\pi\gamma_{\mathrm{FBG}} \sin\left[\frac{\pi}{4}(k + 1/2)\right]}. \tag{A15}$$

For $k = 0$, we obtain $L^k_{\mathrm{c,FBG}} \approx 10$ mm.

We have studied the complex functions $\hat{F}(\widetilde{\delta\lambda_r})$, $\hat{G}(\widetilde{\delta\lambda_r})$ and their sum $\hat{K}(\widetilde{\delta\lambda_r})$. The behavior of these functions in the complex plane for sensor #1 is exemplified in Fig. 7 by plots for OPDs of 6.9 and 12.9 mm, the values used in the experiments (section 4.2 of the main text). Similar plots have been obtained for sensor #2. The values of the other parameters used in obtaining the functions are given in the figure caption. It can be seen that $\hat{F}(\widetilde{\delta\lambda_r})$ and $\hat{K}(\widetilde{\delta\lambda_r})$ resemble a circle arc, whereas $\hat{G}(\widetilde{\delta\lambda_r})$ is like a short line segment given by $\mathrm{Re}\{\hat{G}(\widetilde{\delta\lambda_r})\} \approx$ constant. Resulting from a single period of $\widetilde{\delta\lambda_r}(t) = \delta_0 \sin(2\pi f_0 t)$, where $\delta_0 = 40$ pm is a typical amplitude in the experiment, the arcs and line segments are symmetric with respect to the real axis.

$\hat{F}(\widetilde{\delta\lambda_r})$ would be a circle arc if it were given by solely the factor $\exp(i\xi\widetilde{\delta\lambda_r})$, implying that deviation from an arc is due to the envelope $\hat{E}(\widetilde{\delta\lambda_r})$. To visualize the deviation, Fig. 7 also shows

Optics EXPRESS

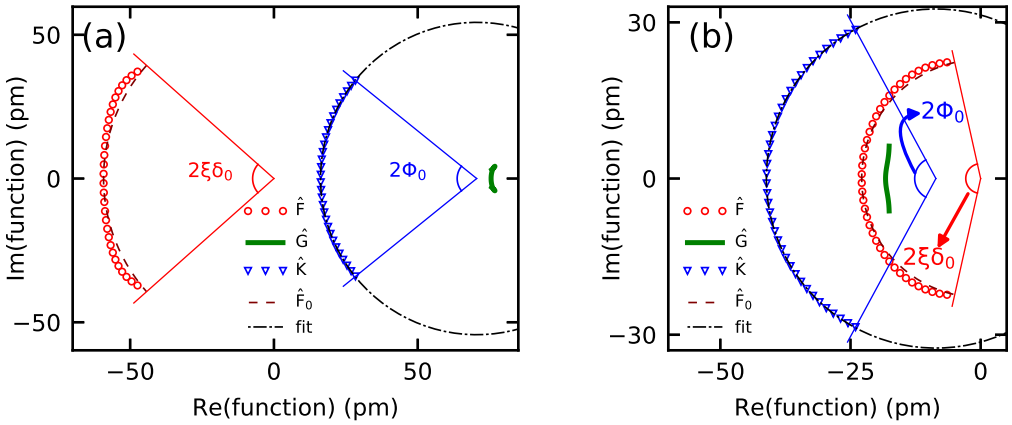

Fig. 7. Plots of the functions $\hat{F}$, $\hat{G}$, $\hat{K}$ and $\hat{F}_0$ in the complex plane for (a) OPD=6.9 mm and (b) OPD=12.9 mm. Zero angular deflection of the functions occurs for the point where Im(function)=0. The black dash-dotted curve is a fit of a circle to the data points of $\hat{K}$, giving radii of 54.3 and 32.6 pm for the OPDs of 6.9 and 12.9 mm, respectively. For $\hat{F}_0$ the radii are 60.1 and 23.2 pm, for these OPDs. In the plot the total bi-directional angular deflections $2\xi\delta_0$ and Φ_0 for the functions $\hat{F}_0$ and $\hat{K}$, respectively, are indicated. In calculating the functions, the following parameters were used: $\gamma_r = 122$ pm, $\gamma_{\mathrm{FBG}} = 207$ pm, $\varepsilon = 0.043$ (the three values in section 2 for sensor #1) and $\delta_0 = 40$ pm.

the circle $\hat{F}_0(\widetilde{\delta\lambda_r}) = R_{F0}\exp\{i\xi\widetilde{\delta\lambda_r}\}$, defined by the radius $R_{F0} = \hat{E}(0)$. Deviation form a circle is present for either OPD, albeit most clearly for OPD = 6.9 mm.

The rather close resemblance of the sum $\hat{K}(\widetilde{\delta\lambda_r}) = \hat{F}(\widetilde{\delta\lambda_r}) + \hat{G}(\widetilde{\delta\lambda_r})$ to a circle arc for either OPD suggests as a first approximation

$$\hat{K}(\widetilde{\delta\lambda_r}) = \hat{E}(\widetilde{\delta\lambda_r})e^{i\xi\widetilde{\delta\lambda_r}} + \hat{G}(\widetilde{\delta\lambda_r}) \cong \hat{F}_0(\widetilde{\delta\lambda_r}) + z_0 = R_{F0}e^{i\xi\widetilde{\delta\lambda_r}} + z_0. \tag{A16}$$

Here $z_0 = |z_0|\exp(i\varphi_{z0})$ is the circle center's coordinate, which in this approximation can be taken constant and real. Eq. (A16) for the function $\hat{K}(\widetilde{\delta\lambda_r})$ has a simple geometrical interpretation: the product $\xi\widetilde{\delta\lambda_r}$ is as the instantaneous angular deflection of the periodic motion of the point $\hat{K}(\widetilde{\delta\lambda_r})$ on the circle arc, induced by the ultrasound. In Fig. 7 the dash-dot circles through the data points of $\hat{K}(\widetilde{\delta\lambda_r})$ are fits of a circle to these points, where the circle is given by the right hand side of Eq. (A16) but R_{F0} is now treated as a fit parameter. Very close similarity to a circle is quantified by the average deviation of 0.1% of the points from the circle.

Although the approximation given by Eq. (A16) and the periodic motion on the circle arc already present the physics picture, refinement is needed, since the functions $\hat{E}(\widetilde{\delta\lambda_r})$ and $\hat{G}(\widetilde{\delta\lambda_r})$ are not constant and thus distort $\hat{K}(\widetilde{\delta\lambda_r})$. Further, $\hat{E}(\widetilde{\delta\lambda_r})$ and $\hat{G}(\widetilde{\delta\lambda_r})$ contribute to the angular deflection on the curve $\hat{K}(\widetilde{\delta\lambda_r})$, modifying the total bi-directional deflection angle $2\xi\delta_0$ on $\hat{F}_0(\widetilde{\delta\lambda_r})$ to the value $2\Phi_0$ on $\hat{K}(\widetilde{\delta\lambda_r})$. In Fig. 7 the deflection angles have been indicated. Φ_0 is the amplitude of the periodic deflection $\Phi(t) = \Phi_0\sin(2\pi f_0 t)$ for $\hat{K}(\widetilde{\delta\lambda_r})$. Assuming that the sensor operates in the linear response regime, characterized by small membrane deflections and small resonance-wavelength modulation compared to the width of the FBG spectrum, the instantaneous deflection $\Phi(t)$ is expected to be proportional to $\widetilde{\delta\lambda_r}(t) = \delta_0\sin(2\pi f_0 t)$. δ_0 in turn, is expected to be proportional to the amplitude p_0 of the ultrasound pressure. Fig. 7 shows that $2\Phi_0 < 2\xi\delta_0$, the inequality being marginally observable for OPD = 6.9 mm. The modification of the total deflection angle suggests to introduce a correction factor defined as $\kappa = \xi\delta_0/\Phi_0 > 1$. The angles in Fig. 7 give $\kappa = 1.07$ and $\kappa = 1.26$ for the OPDs of 6.9 and 12.9 mm, respectively. Similarly, for sensor #2, we obtain $\kappa = 1.03$

and $\kappa = 1.16$ for these OPDs, which are some smaller than for sensor #1. This decrease of κ arises from the smaller γ_r of sensor #2 ($\gamma_r = 96$ pm). Ultimately, in the limit where the width of the line shape of the resonance in the integrand of Eq. (A8) goes to zero, it can be shown that $\kappa = 1$.

In the experiments, the sensors are interrogated by measuring the voltages V_i. Based on the considerations leading to Eq. (A12), the V_i are described by the function $\hat{J} = \exp(i\xi\lambda_r)\hat{K}(\widetilde{\delta\lambda_r}) = \exp(i\xi\lambda_r)\left[\hat{F}(\widetilde{\delta\lambda_r}) + \hat{G}(\widetilde{\delta\lambda_r})\right]$. The function $\hat{J}$, via its dependence on $\exp(i\xi\widetilde{\delta\lambda_r})$ or equivalently on $\exp(i\Phi(t))$, in principle contains all information on the ultrasound. From the V_i the following functions are constructed:

$$V_x(t) = 2V_1(t) - V_2(t) - V_3(t), \tag{A17}$$

$$V_y(t) = \sqrt{3}\,(V_3(t) - V_2(t))\,. \tag{A18}$$

In $V_x(t)$ and $V_y(t)$ the contributions from $I_\alpha(t)$ cancel, as these are independent of φ_i (see Eq. (A9)). Actually, $I_\alpha(t)$ *does* give an appreciable contribution to the *total* integral $I_i(t)$, while $I_\alpha(t)$ carries no useful information on $\widetilde{\delta\lambda_r}$ and thus limits the smallest measurable $\widetilde{\delta\lambda_r}$.

We now rewrite $I_{\beta,i}$ of Eq. (A10) in the approximation given by Eq. (A16), using Eqs. (A11)-(A13):

$$\begin{aligned} I_{\beta,i} &= \mathrm{Re}\left\{e^{i(\varphi_i+\psi_e)}\hat{J}\right\} \\ &= \mathrm{Re}\left\{e^{i(\varphi_i+\psi_e+\xi\lambda_r)}\left[\hat{E}(\widetilde{\delta\lambda_r})e^{i\xi\widetilde{\delta\lambda_r}} + \hat{G}(\widetilde{\delta\lambda_r})\right]\right\} \\ &\cong \mathrm{Re}\left\{e^{i(\varphi_i+\psi_e+\xi\lambda_r)}\left[R_K e^{i\Phi(t)} + z_0\right]\right\}. \end{aligned} \tag{A19}$$

Here R_K is used now instead of R_{F0} to emphasize that we are dealing with $\hat{K}(\widetilde{\delta\lambda_r})$. Based on the definition of κ we have $\Phi(t) = \xi\widetilde{\delta\lambda_r}(t)/\kappa$. Using Eq. (A19) and omitting the prefactor q of Eq. (A5), $V_x(t)$ and $V_y(t)$ can be written as:

$$\begin{aligned} V_x(t) &= 3R_K\cos\left(\Phi(t) + \psi_e + \xi\lambda_r\right) + 3|z_0|\cos\left(\varphi_{z_0} + \psi_e + \xi\lambda_r\right) \\ &= 3\mathrm{Re}\left\{\mathrm{e}^{i(\xi\lambda_r+\psi_e)}\hat{K}(\widetilde{\delta\lambda_r})\right\}, \end{aligned} \tag{A20}$$

$$\begin{aligned} V_y(t) &= 3R_K\sin\left(\Phi(t) + \psi_e + \xi\lambda_r\right) + 3|z_0|\sin\left(\varphi_{z_0} + \psi_e + \xi\lambda_r\right) \\ &= 3\mathrm{Im}\left\{\mathrm{e}^{i(\xi\lambda_r+\psi_e)}\hat{K}(\widetilde{\delta\lambda_r})\right\}. \end{aligned} \tag{A21}$$

$V_x(t)$ and $V_y(t)$ oscillate around levels x_0 and y_0, respectively, given by

$$x_0 = 3|z_0|\cos\left(\varphi_{z_0} + \psi_e + \xi\lambda_r\right), \tag{A22}$$

$$y_0 = 3|z_0|\sin\left(\varphi_{z_0} + \psi_e + \xi\lambda_r\right). \tag{A23}$$

Eqs. (A20) and (A21) show that $V_x(t)$ and $V_y(t)$ are orthogonal, a known property [16] for the combinations of outputs of a 3×3 coupler defined by Eq. (A17) and (A18). Further, in time, the point $\left(V_x(t), V_y(t)\right)$ traces a circle arc in the $V_x - V_y$ plane, of radius $3R_K$ and with center (x_0, y_0). Equivalently, the circle arc according to these equations is a plot of the function $3\exp(i\xi\lambda_r + i\psi_e)\,\hat{K}(\Phi(t))$ in the complex plane. Experimentally, measuring $V_x(t)$ and $V_y(t)$ leads to $\Phi(t)$, which yields Φ_0 by Fourier transformation. Details about the interrogation procedure in practice are given in section 4.1 of the main text.

As described in section 3.1, a high pass filter is applied after the TIAs. The signal components x_0 and y_0, which are close to DC in view of the slow drift of the environmental phase ψ_e, will thus be

Optics EXPRESS

removed. However, by rewriting the terms with $\sin(\Phi(t) + \xi\lambda_r + \psi_e)$ and $\cos(\Phi(t) + \xi\lambda_r + \psi_e)$ in Eqs. (A20) and (A21) towards linear combinations of $\sin(\Phi(t))$ and $\cos(\Phi(t))$, and by using Bessel function expansions [23], it can be shown that signal components at the ultrasound frequency f_0 and its harmonics result. These components, which survive the high pass filtering, are modulated by $\sin(\xi\lambda_r + \psi_e)$ or $\cos(\xi\lambda_r + \psi_e)$ and thus still depend on the environmental phase. This is not an issue, since the time scale for interrogation of the sensor is much shorter than the time scale of the drift. Thus, the angular deflection amplitude Φ_0, which is the principal sensor signal, can be obtained.

Appendix B : Modulation method for measuring the amplitude of the resonance-wavelength modulation

The modulation method is based on ultrasound-induced modulation of the transmission of the sensor operated in a point on the steep and linear flank of the transmission dip (see Fig. 2(b)). The laser also used for characterizing the MZI (section 3.2) actuates the sensor and is tuned to the operation point. We measure the modulated power transmitted through the sensor using a photodetector (New Focus, 1811-FC-AC). The resonance-wavelength modulation according to this method is

$$\widetilde{\delta\lambda_r}(t) \approx \frac{T^0_{\text{pass}}(\lambda_{\text{op.}}) - T_{\text{pass}}(\lambda_{\text{op.}}, t)}{\partial T^0_{\text{pass}}/\partial\lambda\big|_{\lambda_{\text{op.}}}} \tag{B1}$$

Eq. (37) implies that $\widetilde{\delta\lambda_r}$ can be obtained from a time trace $T_{\text{pass}}(\lambda_{\text{op.}}, t)$, and from the static transmission value $T^0_{\text{pass}}(\lambda_{\text{op.}})$ and its derivative $\partial T^0_{\text{pass}}/\partial\lambda\big|_{\lambda_{\text{op.}}}$. The latter two quantities follow from a static transmission curve as in Fig. 2(b), which is also measured using the laser setup just described, albeit that the laser wavelength is swept and the DC mode of the detector is used. The modulation amplitude δ_0 is obtained as the peak value of the Fourier transform of $\widetilde{\delta\lambda_r}(t)$ at 1.3 and 0.77 MHz for sensors #1 and #2, respectively.

Funding

Netherlands Organisation for Scientific Research (NWO) (13534); NL Agency; Brazilian Research National Council (CNPq).

Acknowledgments

The authors thank W.J. Westerveld, S. Leinders, M. Verweij, H.P. Urbach and N. de Jong for stimulating discussions. The RR sensors for this work were made available by W.J. Westerveld and S. Leinders, who conceived the design of the sensors, were involved in defining the steps for membrane creation and had the sensors fabricated. E.C. Noothout made available ultrasonic transducers. K.W.A. van Dongen is acknowledged for his initiative towards this MEMPHISII research activity and J. Pozo and D. Lo Cascio for sharing their ideas.